Axial tension/compression and torsional loading of diamond and gyroid lattice structures for biomedical implants: Simulation and experiment

Anatolie Timercan, Patrick Terriault, Vladimir Brailovski *

Department of Mechanical Engineering, École de technologie supérieure, 1100, Notre-Dame West, Montreal, Quebec H3C1K3, Canada

HIGHLIGHTS

- Diamond and gyroid lattices with 750 μm-diameter pores were manufactured from Ti64 within 0–5 % of the targeted 50–60–70–80 % porosities.
- Lattices showed quasi-identical behavior in tension and compression with elastic moduli of 3–22 GPa and yield stresses of 48–186 MPa.
- Shear to axial yield stress ratios for the diamonds (∼0.94) and gyroids (∼0.87) differ from 0.577 for bulk isotropic materials.
- Simulations overestimated the experiments by ∼ 25 % given the limitations related to boundary conditions and manufacturing defects.
- Studied lattices exhibited adequate resistance for the use in intervertebral cages and stiffness situated in the range of bone properties.

GRAPHICAL ABSTRACT
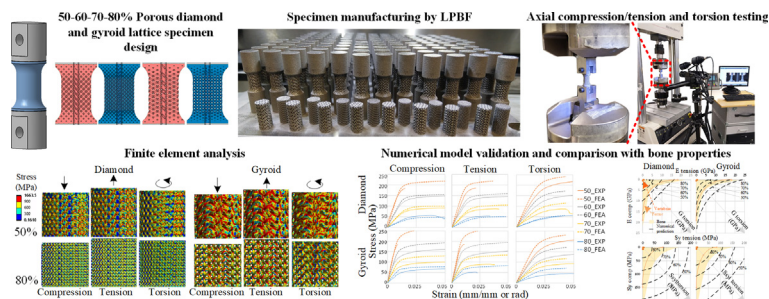
ARTICLE INFO

ABSTRACT

Lattice structures are increasingly used in biomedical implants, notably intervertebral cages, requiring a better understanding of their behavior for the different types of loading they undergo during application. Strut-based diamond and sheet-based gyroid structures with porosity levels ranging from 50 to 80 % and an identical pore size of 750 μm were manufactured from Ti6Al4V alloy, tested experimentally and simulated numerically in axial tension/compression and in torsion to simulate flexion/extension, compression and rotation of the human spine. The manufactured structures were within 5 % of the targeted porosity. However, numerical simulations overestimated the experimental apparent (effective) stiffness and strength of the structures by an average of 25 %, likely due to the presence in them of manufacturing defects, especially in the higher porosity lattices. Experimental and numerical results showed that the structures have quasi-identical mechanical properties in compression and in tension. However, a comparison of the torsion and axial results indicated that conventional bulk material failure theories such as the von Mises limitation criterion do not apply to the apparent properties of lattice structures.

---

* Corresponding author.

E-mail addresses: anatolie.timercan.1@ens.etsmtl.ca (A. Timercan), patrick.terriault@etsmtl.ca (P. Terriault), vladimir.brailovski@etsmtl.ca (V. Brailovski).

Studied lattices exhibited adequate resistance for use in intervertebral cages, however their stiffness was greater than those of the vertebrae, while situated in the stiffness range of cortical bone.

1. Introduction

Recent accessibility of high-end additive manufacturing (AM) systems and their increased use in industry have resulted in more widespread applications. Particularly of interest is the use of AM systems to produce complex geometries that cannot be obtained using traditional machining or forming methods. Biomedical applications are particularly well-suited to take advantage of the design freedom offered by AM through the use of biomimicking structures. Lattice structures have been successfully employed in biomedical implants to simultaneously reduce implant stiffness and promote tissue ingrowth, both leading to more stable fixation at the operation site [1–5]. Titanium, one of the most used metals to manufacture biomedical implants, has an elastic modulus of ~ 110 GPa which is considerably higher than the elastic modulus of bone (7–30 GPa) [6]. Through the use of lattices, the apparent (effective) modulus of elasticity of titanium structures can easily be reduced to that of the bone range [3,5]. Many types of lattice structures are under investigation for biomedical applications, ranging from stochastic to ordered and from homogeneous to graded, with unit cells varying from strut-based to network (skeletal)-based and sheet-based [7]. There is growing interest in triply periodic minimal surface (TPMS) structures due to their increased mechanical properties as compared to their strut-based lattice equivalents [4,8,9]. To adequately design devices integrating lattice structures and ensure their resistance and longevity, it is necessary to understand the mechanical properties and behavior of these lattice structures under real-life loading conditions.

Most research regarding the mechanical properties of lattice structures focus on compression testing since it is the simplest to perform and does not require specialized testing setups [10–17]. However, under real-life conditions, these structures are also submitted to tensile, torsional, and combined loading cases for which the structures' mechanical response must be known. Some efforts have been deployed to characterize lattice structures under more than one loading mode. Yu, Li, Li, Zhang, Hua, Liu, Zhao, Dhaidhai, Li and Wang [18], compared sheet-based TPMS and strut-based structures under tension and compression and found that the former structures yield higher strengths and stiffnesses than the latter. For all the structures, while the elastic moduli in tension and compression were found to be nearly identical, the compressive strength proved to be approximately 1.5 times higher than the tensile strength. Kelly, Francovich, Julmi, Safranski, Guldberg, Maier and Gall [19] reported that the tensile stress–strain diagrams of sheet-based gyroid TPMS structures did not exhibit inflection points corresponding to the onset of plastic deformation contrary to compression for which plateau and densification regions could be observed. Furthermore, under monotonic testing conditions, the compressive strength of the TPMS structures was found to be 1.2–2.2 times greater than the tensile strength, this effect being more pronounced under fatigue testing conditions (4.5–11.5 times). The number of works that also investigate torsional loading of lattice structures is much smaller. Among them, Yánez, Cuadrado, Martel, Afonso and Monopoli [20] conducted static compression and torsion tests on network-based gyroid structures, finding that the compressive and shear properties are very close in terms of the elastic moduli and ultimate strengths. Nelson, Kelly and Gall [21] is the only identified study that contains results on

the mechanical behavior of lattice structures under more than two simple testing modes: tension, compression, torsion and compressive shear. Their findings indicate that the TPMS structures are stronger and stiffer than their strut-based equivalents across all the loading modes. However, since this study is limited to experimental testing and the different loading modes used varying specimen designs, comparison between the stress-states for the same lattice type proved challenging. They concluded that a universal specimen design must be developed to allow adequate comparison of the mechanical behavior for different loading modes.

Numerical simulations using finite element analysis (FEA) constitute an alternative to costly experimental testing to characterize the behavior of components subjected to different loading conditions. When calibrated correctly, they have been proven to be a powerful tool. The simulation of lattice structures presents a great challenge due to their geometric complexity, requiring fine meshing, and therefore, large computational resources [22]. The two most used approaches for FEA of lattice structures are direct simulations, where the entire structure is modeled, and analyses by homogenization, where solid elements with lattice-equivalent properties are used. The former method is more appropriate in cases where the local behavior of structures must be studied, while the latter is preferred for simulating the behavior of large components incorporating significant volumes of lattice structures [23]. Combining the two approaches allows a multiscale modeling of such constructs. The most recent efforts on lattice FEA use direct simulations and can be separated into two levels of analysis, the first calculating the stress distributions inside lattice structures [18,24] and the second, calculating the apparent properties of these structures [10,11,15,16,25,26]. Generally, the mechanical properties of lattice structures predicted by numerical simulations differ significantly from their experimental equivalents, with some models overestimating the actual properties [10,11], and others, underestimating them [15,26]. These differences are explained by the presence of manufacturing-induced geometric deviations, internal defects and surface roughness [10,15,16,26].

To sum-up the preceding, few studies have been carried out on the mechanical response of lattice structures under more than one loading mode, and to the authors' knowledge, no studies have compared simulations and experiments of various lattice structures under different loading modes. This study aims to partially fill this gap by studying the monotonic axial tension/compression and torsional mechanical behavior of two lattice structures, strut-based diamonds and sheet-based TPMS gyroids, which could be considered representative, respectively, of rod- and plate-based trabecular bone structures [27]. Both structure types were manufactured by laser powder bed fusion from Ti6Al4V alloy powder with a constant pore size of 750 μm and a porosity level ranging from 50 to 80 %, with both characteristics selected in accordance with the recommendations for improved osseointegration [28–31]. Numerical models were built for each type of the lattice structures, each level of porosity and each loading mode, and partially validated by comparing the numerical and experimental results. The mechanical properties for the three loading modes that simulate flexion/extension, compression and rotation of the human spine were assessed and compared to the properties of bony tissues and the functional requirements of intervertebral cages.

2. Materials and methods

2.1. Specimen design and manufacturing

A proprietary *MATLAB (MathWorks, Massachusetts, USA)* algorithm was used to create the diamond structures using hexagonal prisms as struts to facilitate meshing [32]. A more detailed explanation of the parameter selection and structures design can be found in the previously published study [6]. Gyroid structures were generated using *nTopology (nTopology, New York, USA)* software. Table 1 summarizes the selected geometric parameters of both structures and the expected porosity levels.

The specimens used in this study were designed to allow their compression, tension and torsion testing and their design was loosely based on that of standard cylindrical dog-bone test specimens (Fig. 1 – Type 1). All the specimens featured a central gauge part with constant porosity and cross-section, solid end pieces that interfaced with the materials testing machine, and transition zones connecting the two. The transition zones with decreasing porosity and increasing cross-section allowed a gradual connection between the studied lattice structure and the fully dense end pieces (Fig. 2). Moreover, to allow sound torsional testing, the central part of the specimens was designed as a hollow cylinder with an outer diameter of 10 mm and inner diameter of 2 mm. The height of the region of interest was set to 10 mm. These dimensions ensured that at least one complete unit cell filled the specimen wall thickness for all selected structures. In addition, the selected geometry was the result of a compromise between the compression testing requirements (height = 1–2 × diameters), torsion testing requirements (height = 6–8 diameters) and manufacturing considerations, such as the minimum feature thickness and total specimen height [33,34]. Although not without any drawbacks, the universal specimen design presents a good compromise between the requirements for compression, tension and torsion testing and must allow adequate comparison between lattice response to the three loading modes. Finally, solid end pieces featured two flat parallel surfaces and transversal holes which, when used in conjunction with pins and adapters for the MTS machine, allowed the application of tensile and torsional loads, in addition to compression. For more precise and detailed experimental verification of manufactured porosities using the ASTM F2450-18 standard [35], a second type of specimens in the shape of plain cylinders with a 10 mm diameter and 20 mm height was also designed (Fig. 1 – Type 2).

A total of 120 Type 1 specimens (15 per porosity level) and 16 Type 2 specimens (2 per porosity level) were manufactured using an *EOS M280 (Krailing,Germany)* laser powder bed fusion system (Fig. 3). Ti6Al4V alloy powder (particle size distribution d_{10} = 24 μm, d_{50} = 44 μm and d_{90} = 61 μm) from *GE Additive (Boisbriand, Canada)* was used and the default *EOS* printing parameters for 30 μm layer Ti64 were employed. The scanning strategy for the part infill was stripe hatching with a 67° rotation between succeeding layers, laser power 280 W, scanning speed 1200 mm/s and hatching distance 140 μm; contours were scanned with a 150 W laser power and a 1250 mm/s scanning speed. It is important to note that for the most porous gyroid structure (∼80 %), contour printing parameters were primarily applied, since the walls thickness was too small for the infill scanning strategy (Fig. 4). To ensure that manufactured specimens respected the design

Table 1

Parameters of the studied diamond and gyroid lattice structures having a target pore diameter of 750 μm.

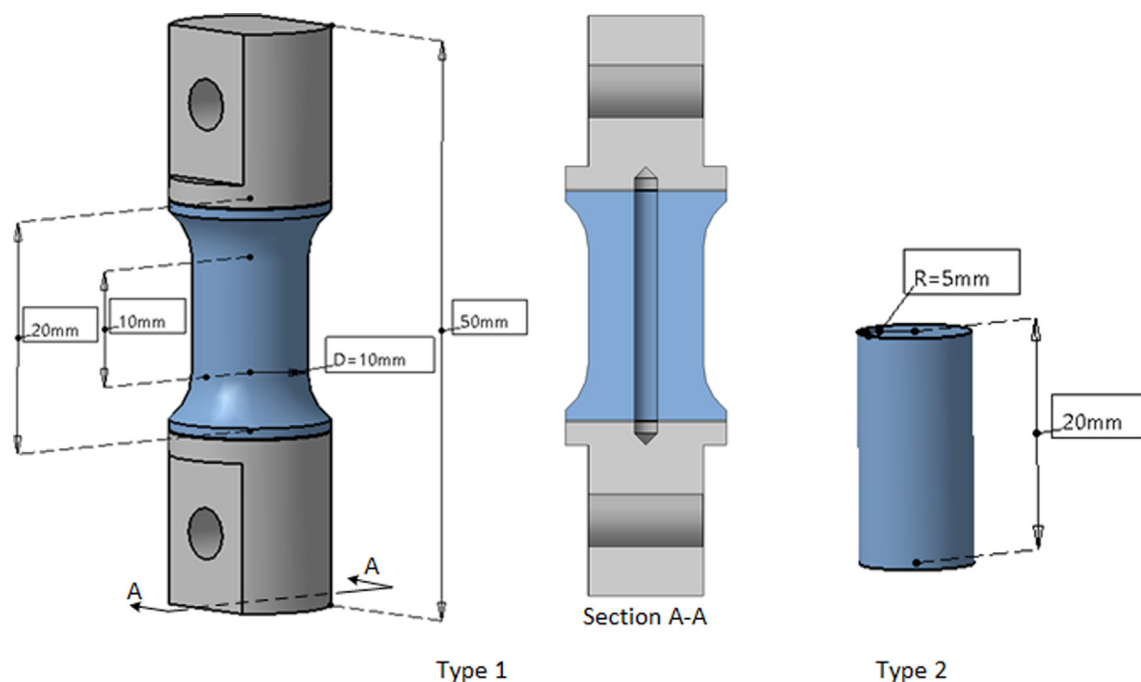|	Strut/sheet thickness [μm]	Cell size [μm]	Designed porosity [%]
Diamond	586	1663	50.1
	455	1485	59.9
	345	1336	69.8
	240	1193	80.4
Gyroid	430	2754	50.6
	305	2431	61.4
	210	2191	70.5
	125	1977	81.3

Fig. 1. Specimen designs and overall dimensions: Type 1 used for mechanical testing and Type 2 used for porosity verifications. Areas in blue indicate porous parts of the specimens. (For interpretation of the references to colour in this figure legend, the reader is referred to the web version of this article.)
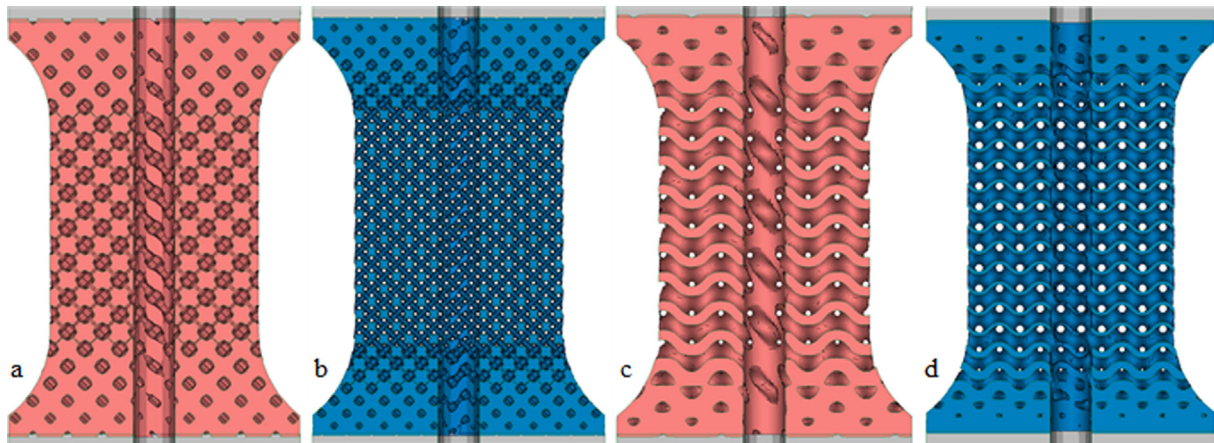
Fig. 2. Central parts of the diamond (a,b), and gyroid (c,d) structures with a porosity of 50% (a,c) and 80% (b,d).
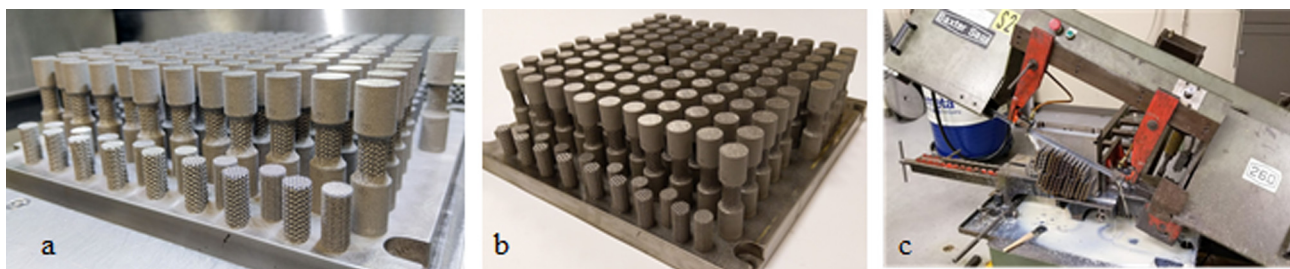

Fig. 3. Specimens on the build plate after (a) manufacturing and (b) removal from machine; (c) specimens separation from the build plate.
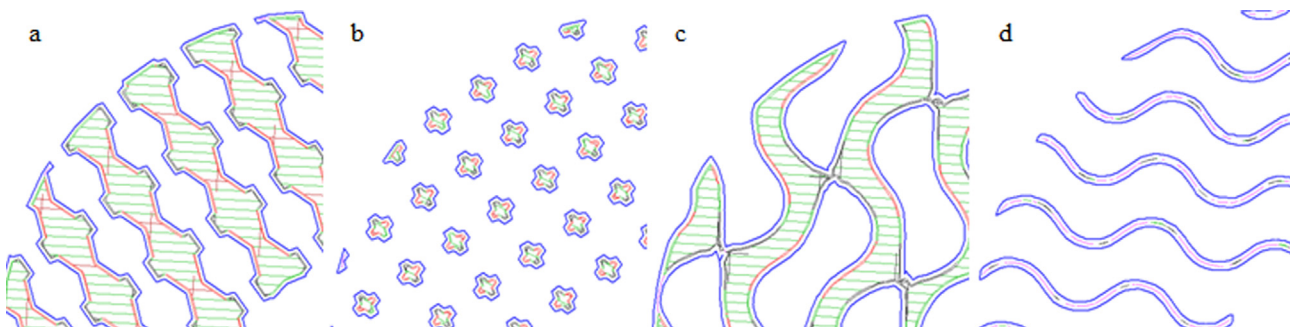

Fig. 4. Scanning strategy for the diamond (a,b), and gyroid (c,d) structures with a porosity of 50% (a,c) and 80% (b,d). The blue outline indicates the structure cross-section, green lines indicate infill scanning, red and black lines are upskin and downskin areas, respectively, and contouring is shown in pink. (For interpretation of the references to colour in this figure legend, the reader is referred to the web version of this article.)

requirements as closely as possible, the AM system-specific laser beam offset was determined for the two types of structures (35 μm for diamond and 20 μm for gyroid). After printing, a stress relief heat treatment of 800 °C for 4 h under inert atmosphere was carried out. The specimens were then separated from the build plate by means of bandsaw cutting. Supports were removed and functional surfaces machined to ensure adequate fit with the testing apparatus. All the specimens were cleaned in an ultrasound bath for 30 min to remove any remaining loose powder and cutting oil. One sample of both the diamond and gyroid specimens (Type 1) of each porosity level were scanned using a *Nikon XTH225 (Tokyo, Japan)* computed tomography (CT) system to verify their geometric conformity, structural integrity and the absence of debris inside the lattice. The scans were carried out with a 192 kV tube voltage, 55 μA current and 12 μm resolution. *CT Pro 3D (Nikon, Tokyo, Japan)* software was used to reconstruct the scans and generate TIFF image stacks that were then imported into *VGStudio MAX*

3.1 (Volume Graphics, Heidelberg, Germany) software and converted into volumes for analysis. The porosity validation plain cylindrical specimens (Type 2) were weighed (*Sartorius Secura 324–1 s* scale, ±0.0001 g) and their diameter and height measured (*Mitutoyo* micrometer ± 0.001 mm). Porosity was calculated according to Equation (1). The material volume was obtained by dividing the specimen mass by the material density (4.43 g/cm^3 for Ti6Al4V) and the total volume was calculated using the diameter and height of the specimens.

$$\varphi\,(\%) = \frac{V_{void}}{V_{total}} * 100 = \left(1 - \frac{V_{material}}{V_{total}}\right) * 100 \tag{1}$$

2.2. Numerical simulations

Concurrently, finite element analyses were carried out on the central constant-porosity portions of the specimens using a work-
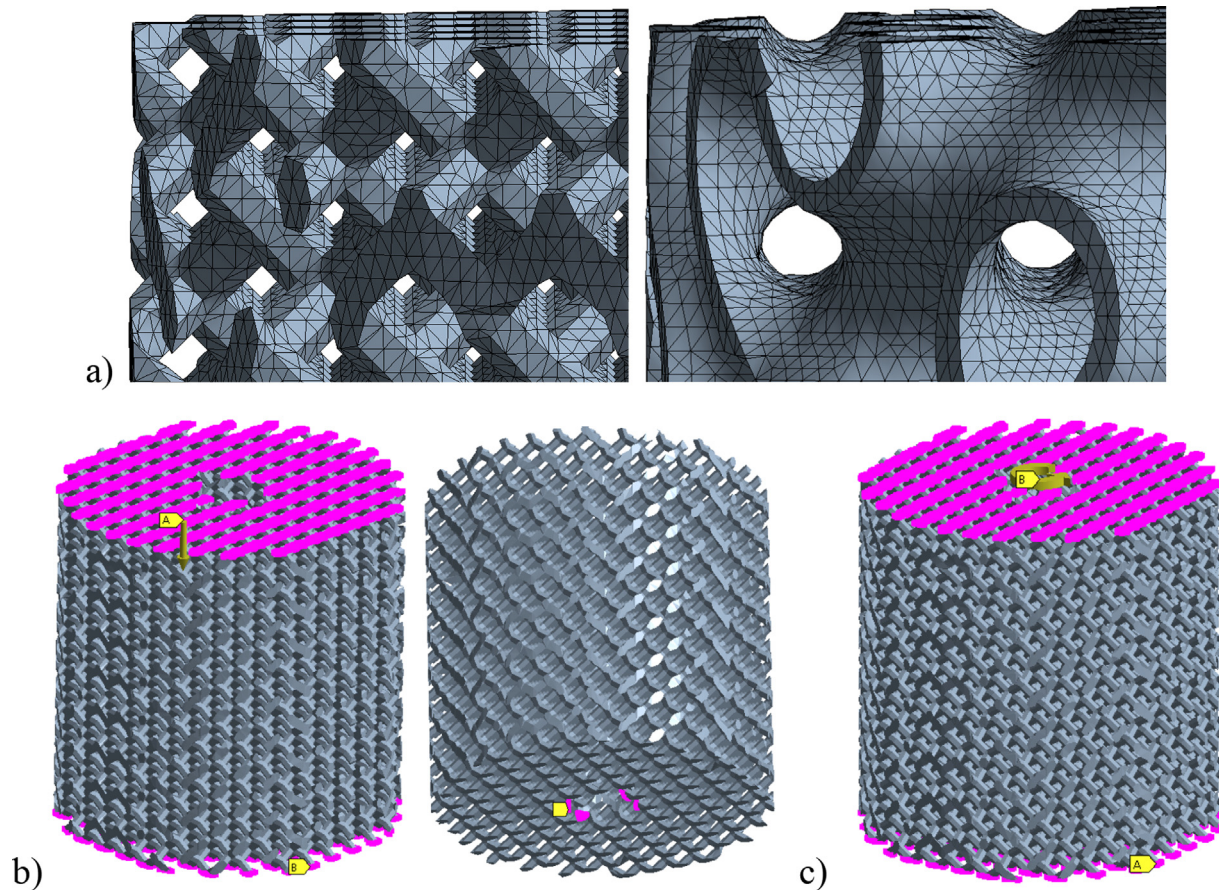
Fig. 5. Mesh details for the diamond and gyroid structures (a) and boundary conditions applied on the 80%-porosity diamond structure in compression (b) and torsion (c).

station with two 14 core Intel Xeon E5-2660 CPUs and 256 GB of RAM. STLs of the central sections with a height of 10 mm were imported into Ansys Workbench 2021R1 where compression, tension and torsion loading modes were simulated with large deformation analyses. The FEA mesh was created using the layered tetrahedrons method with a layer height of 0.1 mm and an element size of 0.1 mm (Fig. 5a). The number of elements varied from $\sim$ 1.5 million for the most porous structures to $\sim$ 3.5 million for the least porous structures. The material properties of Ti6Al4V alloy were applied to the structures using the bilinear kinematic hardening model (E = 110 GPa, E_T = 833 MPa, ν = 0.33, S_y = 900 MPa [36]). Mesh convergence analysis was carried out on the equivalent von Mises stress of the 80 % porosity gyroid structure, since this structure has the thinnest walls and requires the smallest elements to provide adequate geometric conformance. The element size selected with a convergence criterion of 5 % also respected the best practice, which recommends at least 2 elements in the wall thickness of the thinnest feature.

For compression and tension testing, the boundary conditions consisted of displacements directly applied to the structure nodes. The displacements of all bottom surface nodes were set to zero in the axial direction, as were the transverse displacements of the central part of the bottom surface nodes (Fig. 5b). The top nodes' axial displacements were applied using automatic stepping up to 5 % apparent strain, with an average of 20 steps to resolve. For torsional testing, the bottom displacements were set to zero in all directions and the rotation was applied using automatic stepping up to 4 % apparent shear strain as remote displacements of the top surface nodes using rigid behavior (Fig. 5c). The reaction force and reaction moment probes were applied to the blocked displace-

ments and then converted to compression/tensile and shear stresses using, respectively, the specimens' cross-section areas and the polar moments of inertia. The resulting stress–strain data were used to calculate the structures' apparent modulus of elasticity and yield stress. In addition to calculating the stress–strain data, the simulations were also used to calculate the material volume fractions under different states of stress. To this end, a script was written using the Ansys parametric design language (APDL) commands tool and was used to select the elements in different stress states (elastic, plastic) and extract their relative volumes.

2.3. Experimental testing

Mechanical testing was carried out on an 858 MiniBionix II MTS system using a 15 kN-150 Nm axial–torsional load cell. Three specimens of each type of structure were tested for each loading mode: compression, tension and torsion, for a total of 9 tests for each structure and porosity level. Separate specimens were used for each test. Loading was applied by increasing the axial increments by 0.5 mm at a rate of 0.01 mm/s and the torsional increments by 5° at a rate of 0.115°/s, until structure failure. For torsional testing, the axial control was set to "floating mode" to prevent additional loading of the structure caused by axial expansion or contraction. Axial forces and displacements, torsional torques and angles were acquired at a rate of 40 Hz. A digital image correlation (DIC) system *Aramis 5 M (GOM mbH, Braunschweig, Germany)* was used as a digital extensometer to measure displacements and strains of two points in the central constant porosity part of the specimens at a rate of 1 Hz (Fig. 6). The data obtained were synchronized and post-treated in *MATLAB*, and then converted to a

Fig. 6. A mechanical testing setup with a digital image correlation apparatus.

stress–strain format to extract the modulus of elasticity, yield and peak stresses apparent values. The modulus of elasticity was obtained during the unloading phase of the tests by fitting a linear equation to the largest portion of data, while maintaining a correlation of ∼ 99 %. This approach was favored in order to minimize the effects of the pin clearance in the apparatus assembly on the specimen stiffness which was observed during the initial loading phase.

3. Results

3.1. Geometric conformance

The porosity of the plain cylindrical specimens obtained by weight measurements was generally within 2 % of the target, except for the highest porosity levels where the deviation reached up to 5 % (Fig. 7a). For all porosity levels, the porosity values obtained from the CT analyses were systematically lower (1–2 %) than the ones measured using the specimen mass and volume. The geometric conformity analysis indicated that for all the specimens, at least 90 % of the total structure surface was within ∼ 80 μm of deviation from the CAD, which is acceptable, given the printing resolution of 80 μm. The deviation distributions

between the actual and CAD surfaces were not symmetrical with respect to zero, as illustrated in Fig. 7b. Although the mean deviations for all structures were close to zero, the peaks of the deviation distributions ranged from −13 μm to + 5 μm, and only structures with the highest (∼80 %) porosity had positive deviation peaks (Fig. 7b). At higher porosities, where the strut/sheet thickness was of the same order of magnitude as the laser beam diameter, manufacturing-induced defects such as pores, geometrical discontinuities and structural distortions were observed (Fig. 8). The gyroid structures exhibited more defects than their diamond equivalents, as expected from their thinner features: 125 μm walls for the former vs 240 μm struts for the latter.

3.2. Numerical simulations

Numerical models predict quasi-identical mechanical behaviors for both structures in compression and tension at all porosity levels (Fig. 9). The gyroid structures are expected to have 1.4–2.7 times higher apparent elasticity moduli as well as 1.1–1.7 times higher apparent yield stresses than their diamond equivalents (Table 2). In torsion, both structures perform identically for the same porosity levels, except for the most porous lattices where the gyroids are 1.4 times stiffer and more resistant than the diamonds (refer to
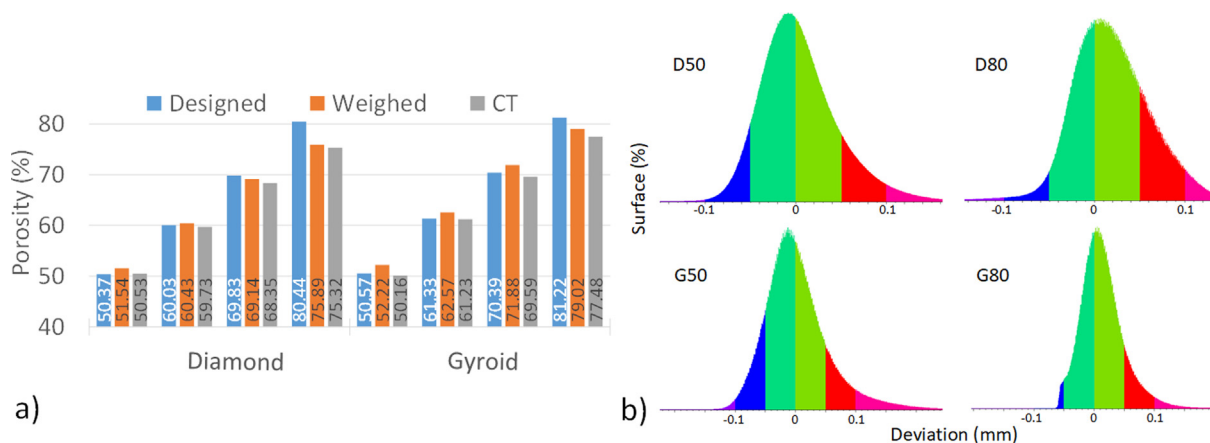

Fig. 7. (a) Porosity levels of the designed and manufactured structures; (b) Surface deviation distributions of the 50% and 80% porous diamond (D) and gyroid (G) structures.
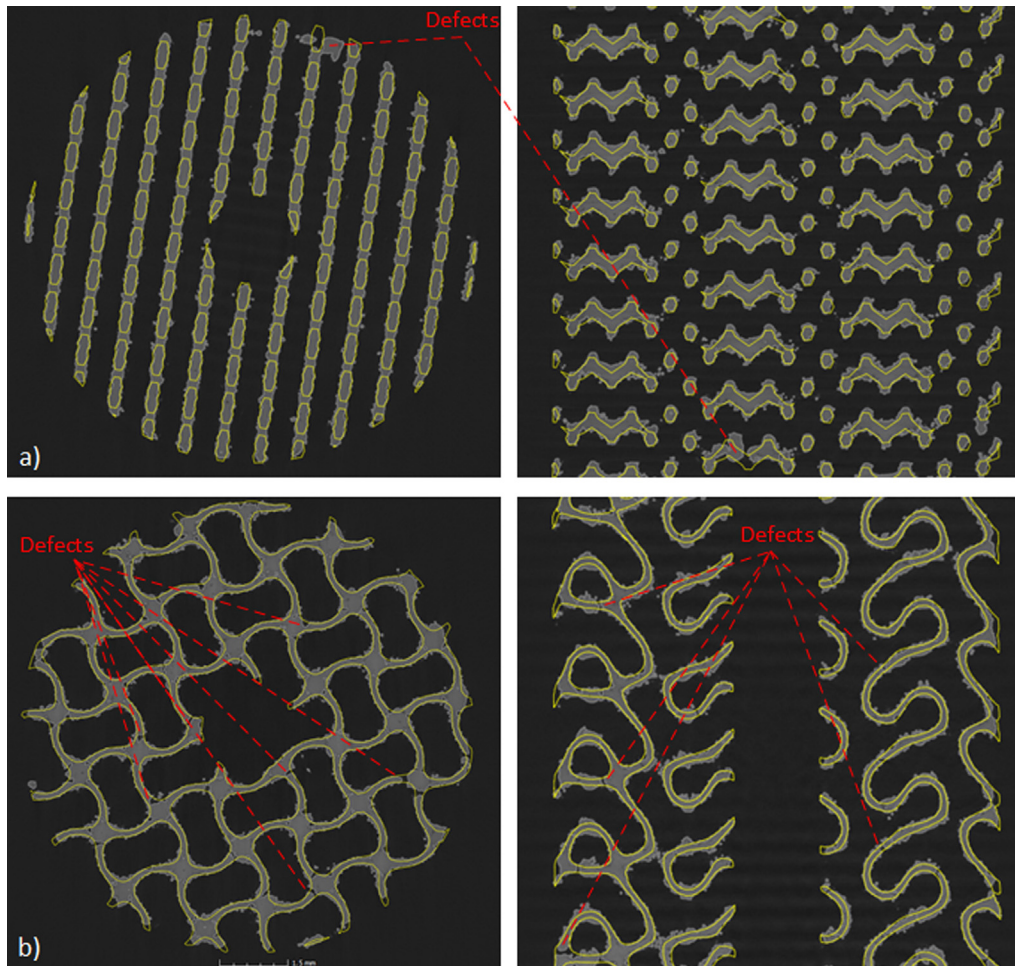
Fig. 8. Manufacturing-induced defects in the most porous (~80 %) diamond (a) and gyroid (b) structures and comparison to the idealised CAD outlined in yellow. (For interpretation of the references to colour in this figure legend, the reader is referred to the web version of this article.)
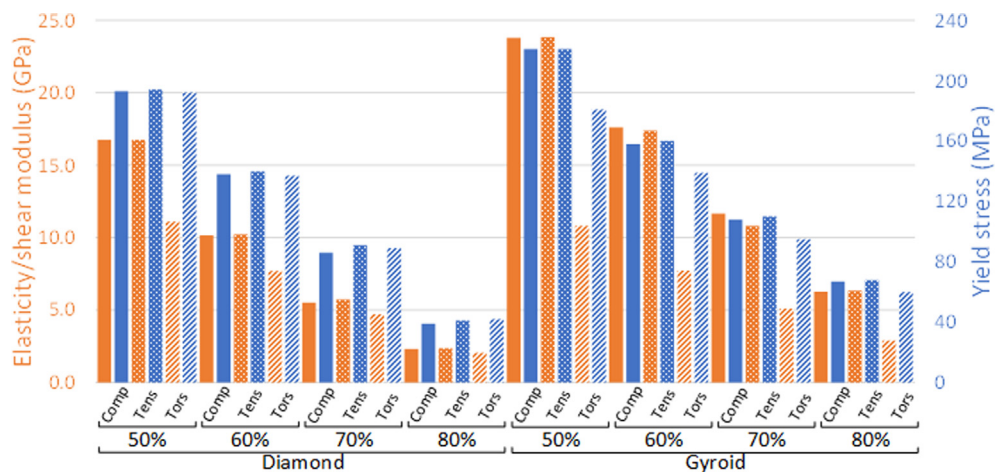

Fig. 9. Numerically predicted apparent mechanical properties: elasticity/shear moduli and yield stresses.

values in Table 2). Stresses in the gyroid structures are more evenly spread compared to the diamond structures where the matter is subjected to more concentrated stresses (Fig. 10). At the same global strains, the volume fractions of matter with stresses exceeding the onset of the yield stress (900 MPa) are higher for the gyroid than for the diamond structures, and the more porous the struc-

ture, the more pronounced this effect (Table 2). That means that under the same global displacements, the gyroid structures will contain more plastically, and therefore, irreversibly deformed matter than their diamond equivalents. It is noteworthy that the stress concentrations in the diamond lattices are at the strut junctions, as often cited in the literature [18]. For the gyroid structures in ten-

Table 2

Numerically predicted apparent mechanical properties: elasticity/shear moduli and yield stresses and volume fractions of the lattice structures undergoing plastic deformation (stresses exceed the bulk material yield stress of 900 MPa) at 5 % of axial and 4 % of torsional global strains.

	Compression			Tension			Torsion		
	E (GPa)	S_y (MPa)	Volume fraction, %	**E (GPa)**	S_y (MPa)	Volume fraction, %	**G (GPa)**	S_{Sy} (MPa)	Volume fraction, %
D50	**16.7**	193	46	**16.8**	194	49	**11.1**	192	29
D60	**10.2**	138	41	**10.2**	140	43	**7.7**	137	21
D70	**5.5**	86	24	**5.7**	91	29	**4.7**	89	13
D80	**2.3**	39	6	**2.4**	41	7	**2.0**	42	2
G50	**23.8**	221	57	**23.8**	221	58	**10.8**	181	35
G60	**17.6**	158	49	**17.4**	160	50	**7.7**	139	28
G70	**11.6**	108	42	**10.8**	110	45	**5.1**	95	22
G80	**6.3**	67	36	**6.4**	68	39	**2.9**	60	17

sion and compression, the maximal stresses are present along helical contours as was also observed by Downing, Jones, Brandt and Leary [37]. It is also worth noting that some isolated and scattered small regions of the lattice are subjected to stresses exceeding the ultimate tensile stress of Ti6Al4V (970 MPa) and their cumulated volume fraction does not exceed 0.5 % of the volume of the entire structure (Fig. 10). This effect is due to the specimen design process where the lattices were cut using a cylinder, leaving not only floating particles (which are removed) but also areas with extremely thin sections acting as singularities. As verified by additional simulations, where these zones were effectively removed ("killed"), such a small number of highly distorted elements bear a negligible impact on the global behavior of these structures and could therefore be ignored.

3.3. Experimental validation

Fig. 11 presents all the experimental (apparent) compression, tension and torsion stress–strain diagrams corresponding to central constant porosity portions of the diamond and gyroid specimens. It is worth noting that for uniaxial loading, i.e., compression and tension, the diamond and gyroid structures with the lowest porosity (∼50 %) reached the testing machine loading limit, and therefore, the specimens did not fail completely. Nonetheless, the onset of plastic deformation was observed and the yield stress calculated. Overall, the repeatability of the lattice mechanical responses was observed for all three specimens tested in each condition. The loading–unloading cycling strains were not identical for the specimens because the overall displacement and the local strains of the porous sections were not always matched from one specimen to the next caused by the assembly clearances. The average experimental apparent elasticity moduli and yield stresses with their standard deviations can be found in Table 3.

Scaling relations in the form of a power law were calculated from the experimental values, allowing the prediction of lattice structure properties as functions of the bulk material properties and the lattice porosity (Table 4). The exponents of the power laws range from approximately 1.6 to 2.3, which are of the same order of magnitude as 2.0 in Gibson, Ashby and Harley [38].

By comparing the experimental and numerical data, it can be observed that the numerical simulations overestimated the elasticity moduli and yield stresses of all the specimens (by ∼ 25 % on average), except for the ∼ 80 % porous diamond structures, where the calculations underestimated these values in compression and tension (∼21 and ∼ 19 %) (Fig. 12). This latter discrepancy is partially explained by the fact that for the highest-porosity diamond structures, the manufactured porosity was ∼ 5 % lower than the designed one, while for the highest-porosity gyroids, this difference was only ∼ 1.5 %. Modeling of the diamond structures was globally closer to the experimental results than the gyroids', with the former having an average relative error of 16 %, and the latter,

of 34 % (Fig. 13). The presence of manufacturing defects, coupled with the uncertainty in the actually obtained porosities, have been noted in the literature as factors that influence the accuracy of the numerical modeling [10,20]. Surface-sintered particles, as can be seen in Fig. 14, affect the density measurements, but do not contribute to the structural integrity of the lattice structures, and therefore introduce errors in the numerical-experimental comparison. Finally, only central parts of the specimens were simulated, thus making the numerical boundary conditions not entirely representative of the experimental testing conditions.

4. Discussion

4.1. Manufacturing of lattices

The difference between the results obtained using two porosity measurement methods, weighting (Archimedes) and CT, although small, can be partly attributed to the thresholding used for the CT. Although the applied automatic thresholding is based on the background and material grey value peaks to determine the matter-void interface, the CT-related effects, such as beam hardening and halo artefacts, can skew the grey value distribution, thus altering the surface determination, and ultimately, the structure volume. In addition, CT scans were performed on the mechanical testing specimens, while the Archimedes measurements were performed on the plain cylindrical specimens; this difference in the specimen shape and size might also partly account for variations in the porosity measurements. Nonetheless, the two measurement methods follow the same trend and inform us of deviations between the designed and manufactured structures. At lower porosities, the printed structures follow the CAD more closely, with deviations increasing alongside the porosity. For both the diamond and gyroid structures, the largest deviations occurred at the highest porosity levels, which are at limits of printability of the LPBF system used in this study. As previously stated, given thin cross-sections of some porous structures, the LPBF system only used contour parameters for printing, with the latter regimes employing lower laser power and higher scanning speed, resulting in smaller energy densities delivered to the powder bed as compared to the infill printing strategy. This can explain some manufacturing defects, particularly geometric discontinuities observed in the ∼ 80 % gyroid structures, where the contour printing parameters were prevalent.

Similar trends were observed by Kelly, Francovich, Julmi, Safranski, Guldberg, Maier and Gall [19], who tried to correct the manufacturing defects (internal voids) by adjusting the printing parameters. While they were successful in reducing these defects, there were still deviations between the manufactured and the designed porosity levels (49 vs 53.9 % and 87 vs 88.1 %). Salem, Carter, Attallah and Salem [39] analyzed the influence of laser power and scanning speed on the geometric conformity and internal
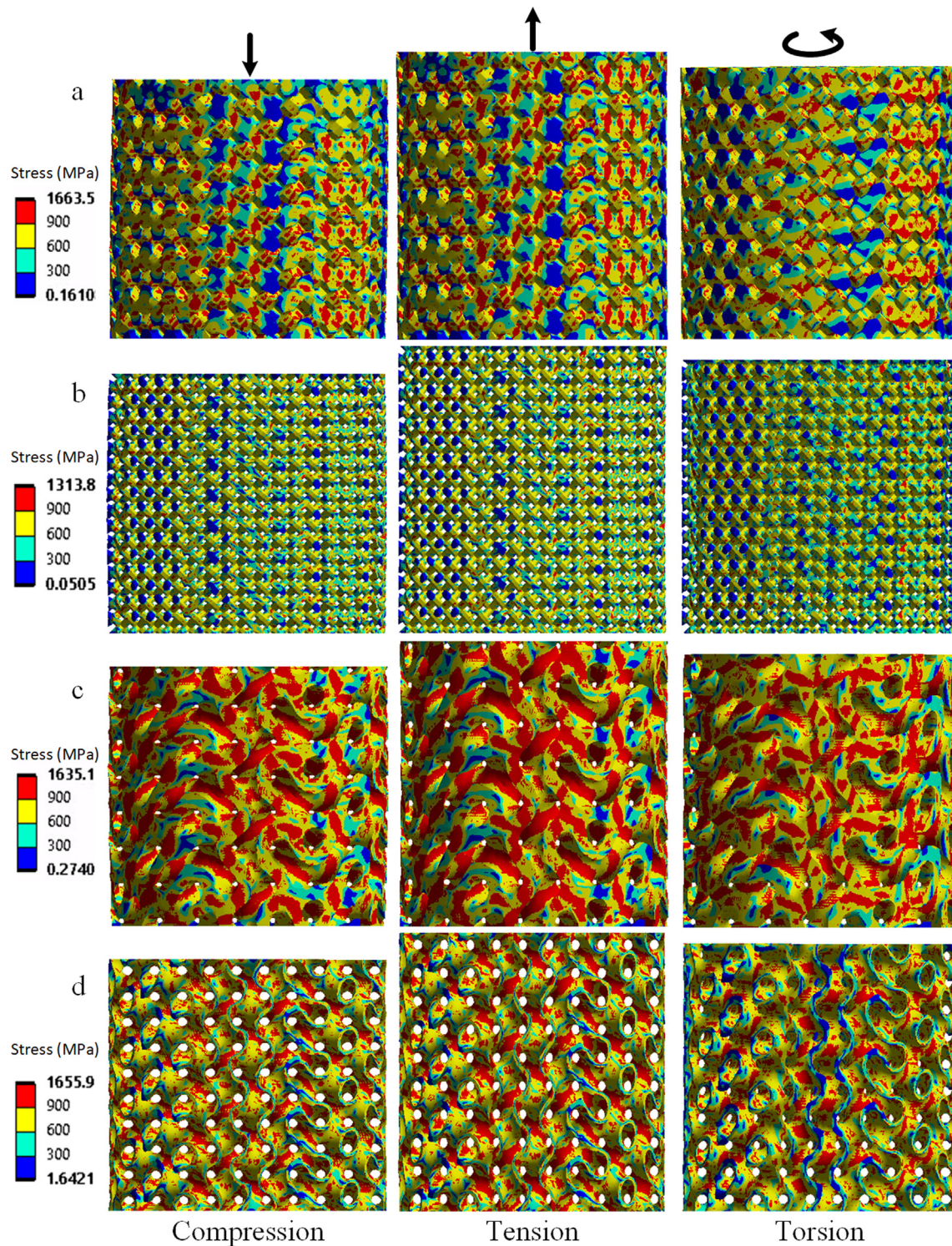
Fig. 10. Simulated stress distributions in the diamond (a, b) and gyroid (c, d) structures at ~ 50 % (a, c) and ~ 80 % (b, d) porosity levels under global strains of 5 % compression, 5 % tension and 4 % torsion.

porosity of a 200 μm strut-thickness Ti6Al4V lattice structure and identified five zones of different manufacturing defects. One parameter set with the lowest tested power (100 W) and one of the lowest tested scanning speeds (1600 mm/s) was identified as the one most closely replicating the CAD and having the least defects. Although the comparison is not straightforward due to the differences in manufacturing systems, this combination of laser power and speed would result in a lower energy density than even

the contouring parameters used in the present work. In addition to the geometric conformity, Sing, Wiria and Yeong [40] also studied the impact of scanning parameters on the mechanical properties, finding that the strut dimensions are most influenced by the laser power whereas the mechanical properties depend not only on the laser power, but also on the scanning speed and layer thickness. This indicates that the printing parameters of lattice structures must be adapted not only to the lattice type, but also to the poros-
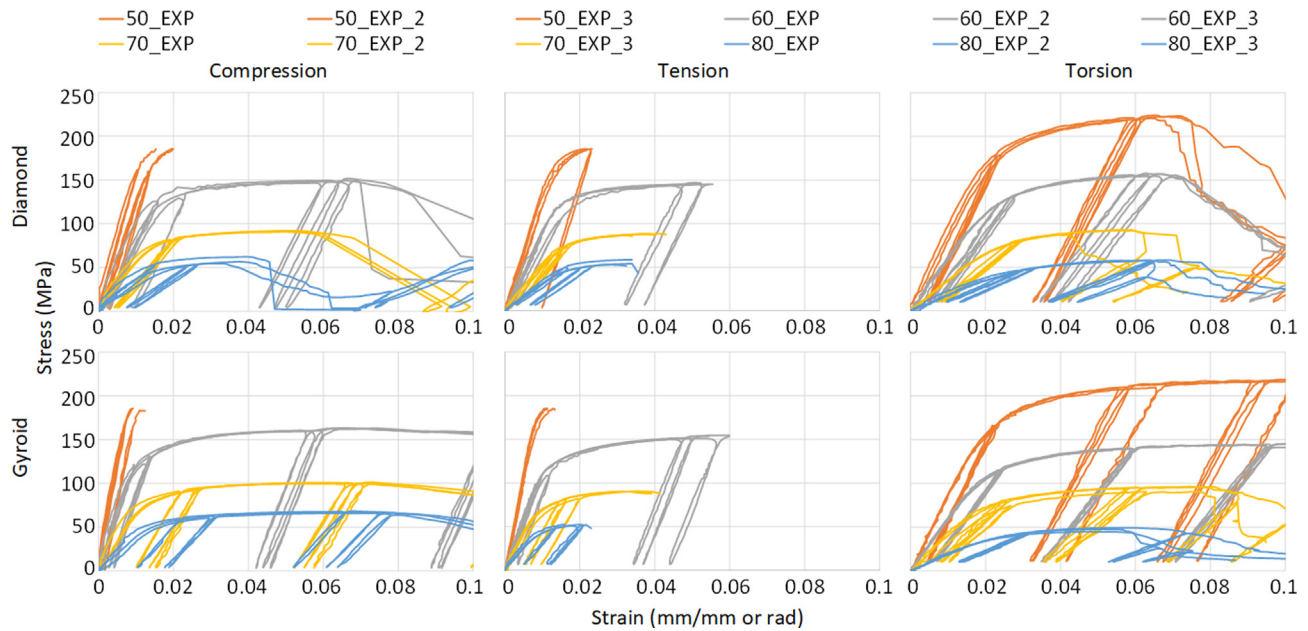
Fig. 11. Stress–strain diagrams of all the experimental tests of the 50, 60, 70 and 80% porosity diamond and gyroid structures under compression, tension and torsion.

Table 3
Experimentally determined (apparent) mechanical properties of the diamond and gyroid structures under compression, tension and torsion.

	Compression		Tension		Torsion	
	E (GPa)	S_y (MPa)	**E (GPa)**	S_y (MPa)	**G (GPa)**	S_{sy} (MPa)
D50 (51.5*)	**15.0 ± 0.05**	173 ± 2.1	**13.8 ± 0.67**	171 ± 2.7	**9.0 ± 0.04**	172 ± 2.2
D60 (60.4)	**9.3 ± 0.56**	122 ± 3.4	**9.4 ± 0.81**	121 ± 2.1	**6.2 ± 0.12**	120 ± 1.1
D70 (69.1)	**5.1 ± 0.08**	75 ± 0.9	**5.3 ± 0.60**	74 ± 0.5	**3.4 ± 0.07**	71 ± 0.6
D80 (75.9)	**3.1 ± 0.25**	48 ± 1.9	**3.0 ± 0.12**	48 ± 3.1	**1.8 ± 0.10**	40 ± 2.1
G50 (52.2*)	**22.0 ± 0.47**	186 ± 3.3	**22.4 ± 0.65**	182 ± 3.1	**8.7 ± 0.14**	162 ± 0.6
G60 (62.6)	**12.6 ± 0.58**	119 ± 1.5	**12.0 ± 0.17**	118 ± 1.9	**5.8 ± 0.22**	106 ± 1.0
G70 (71.9)	**7.6 ± 0.41**	75 ± 1.1	**7.6 ± 0.17**	72 ± 1.0	**3.9 ± 0.20**	71 ± 1.5
G80 (79.0)	**4.8 ± 0.16**	51 ± 1.2	**5.2 ± 0.11**	45 ± 0.6	**1.9 ± 0.02**	36 ± 2.0

*values in parentheses contained in the left column denote the measured porosity levels.

Table 4
Scaling relations of the diamond (D) and gyroid (G) lattice elasticity moduli (E and G) and yield stresses (S_y and S_{sy}) for three loading modes and the corresponding R^2 correlation coefficients.

	Compression		Tension		Torsion	
D	$E_{app} = E * 0.6968*(1 - \varphi)^{2.2773}$	$R^2.998$	$E_{app} = E * 0.6304*(1 - \varphi)^{2.1911}$	$R^2.998$	$G_{app} = G * 1.1196 *(1 - \varphi)^{2.2905}$	$R^2.997$
	$S_{y\_app} = S_y * 0.7458*(1 - \varphi)^{1.8589}$	$R^2.999$	$S_{y\_app} = S_y * 0.7144*(1 - \varphi)^{1.8237}$	$R^2.999$	$S_{sy\_app} = S_{sy} * 1.4755*(1 - \varphi)^{2.0994}$	$R^2.997$
G	$E_{app} = E * 0.7289*(1 - \varphi)^{1.8253}$	$R^2.993$	$E_{app} = E * 0.6802*(1 - \varphi)^{1.757}$	$R^2.978$	$G_{app} = G * 0.7910*(1 - \varphi)^{1.8162}$	$R^2.981$
	$S_{y\_app} = S_y * 0.6413*(1 - \varphi)^{1.5763}$	$R^2.996$	$S_{y\_app} = S_y * 0.6988*(1 - \varphi)^{1.6945}$	$R^2.999$	$S_{sy\_app} = S_{sy} * 1.1285 *(1 - \varphi)^{1.7867}$	$R^2.989$

ity level, considering that modifying the printing parameters to obtain targeted geometries might negatively affect the material microstructure, and therefore, the mechanical properties.

4.2. Mechanical behavior of lattices

In terms of the mechanical behavior, all the manufactured lattice structures exhibit quasi-reversible properties between compression and tension, in agreement with the numerical predictions. Overall, the gyroid structures are stiffer and as strong as the diamond structures under the compressive and tensile loading modes. Looking at the performance in torsion, both structures have almost identical shear moduli and shear yield stresses for similar porosity levels. According to the maximum distortion energy theory, for the bulk material considered homogenous and isotropic, the generally accepted ratio between the shear (S_{sy})

and axial (S_y) yield stresses is 0.577. This ratio can vary for specific alloys and manufacturing techniques. Some studies analyzed bulk Ti6Al4V alloys produced by additive manufacturing and found S_{sy}/S_y to vary from 0.49 to 0.57 [41]. Conversely, on average, this ratio for the diamond structures is 0.94 and for the gyroid, it is 0.87. This difference in the mechanical resistance behavior implies that for the simulation of lattice structures using the homogenization approach [23], the yield criterion of ductile isotropic materials is no longer adequate and alternative criteria, such as Drucker-Prager for example, must be considered. A similar trend was observed for the compression and torsion stiffness and yield stress by Yánez, Cuadrado, Martel, Afonso and Monopoli [20]. In addition, the equation linking the shear and Young's modulus ($E = 2G(1 + \nu)$), which is derived from Hooke's law, can also be considered as not applicable to the lattice structure apparent properties. Applying this formula using the diamond structure moduli results in nega-
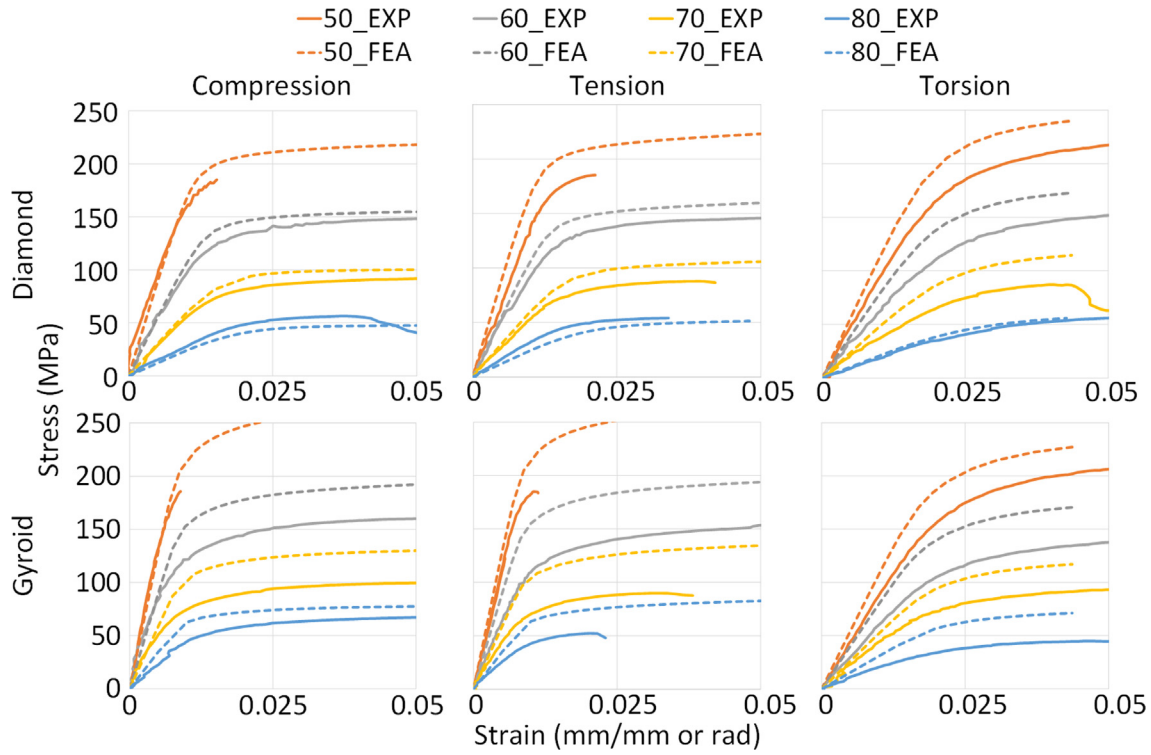
Fig. 12. Comparison of the experimental and FEA stress–strain diagrams (bold lines-experiment, dotted-calculations).
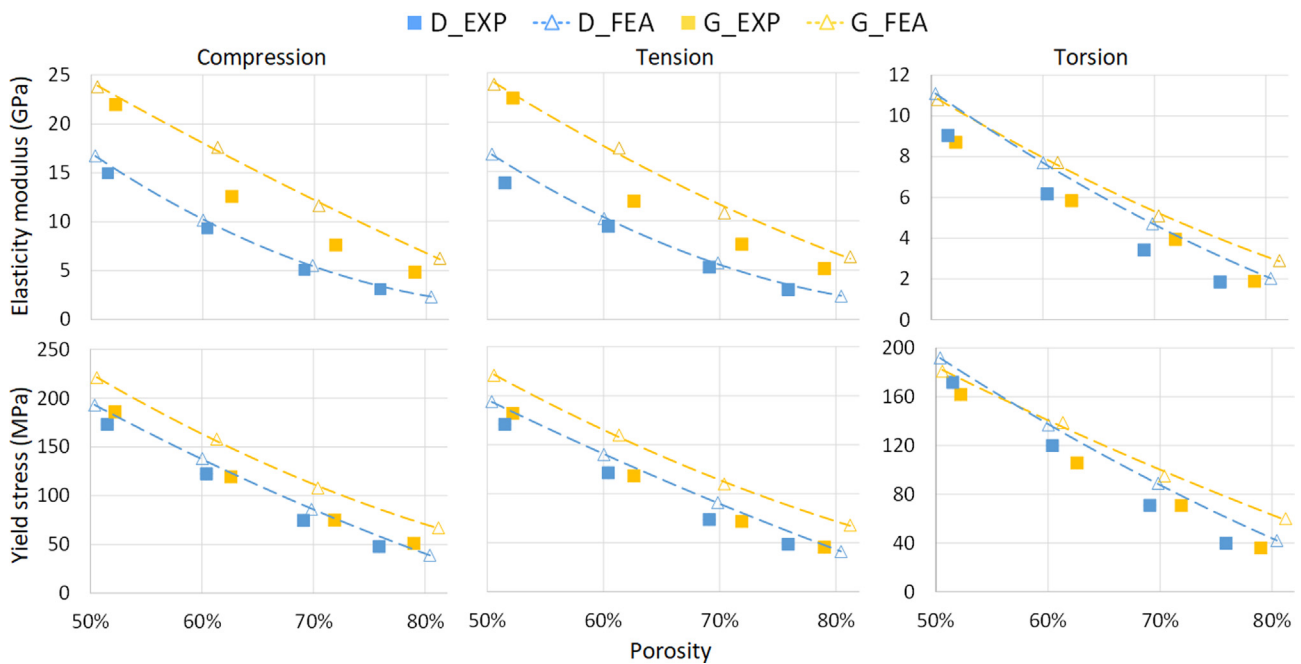

Fig. 13. Experimental (EXP) and numerical (FEA) moduli of elasticity (E) and yield stresses (Sy) as functions of porosity for diamond (D) and gyroid (G) structures in compression, tension and torsion.

tive Poisson's ratios, indicating an auxetic structure, a phenomenon that is not observed numerically or experimentally. Therefore, when simulating lattice structures using the homogenization strategy [23], particular care must be taken when continuous material properties and material behavior are used, given the fact that lattices do not behave as equivalent isotropic materials. While comparison of different lattice types based on the apparent Young's modulus alone remains adequate in cases where only one type of loading is applied to the structure, further analyses are needed to establish a generalized approach to simulate complex elastic behavior of lattice structures.

Although failure occurred in the central portion of all specimens (Fig. 15), a key difference between the two structures is in their failure mode, which is more abrupt for diamonds and more gradual for gyroids. When comparing the scaling relations obtained in this study (Table 4) with those of a previously published work [6], the
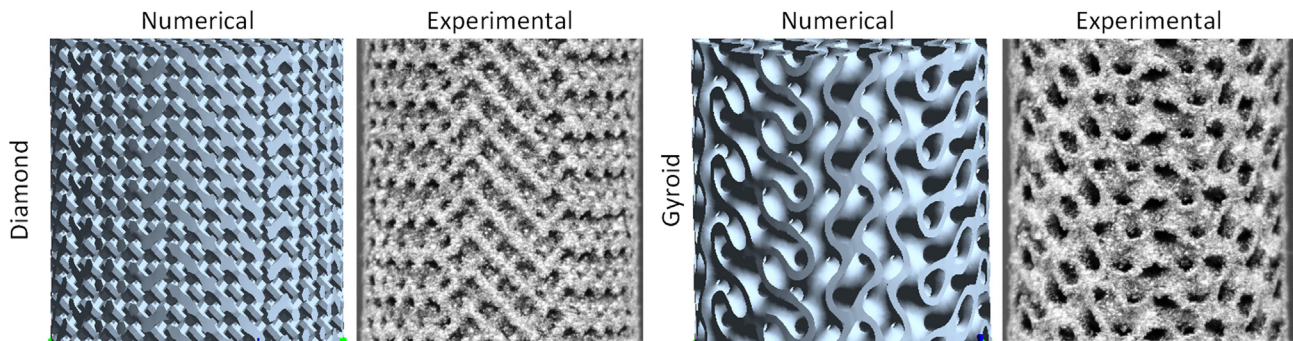
Fig. 14. Comparison of the numerical and experimental 70% diamond and gyroid structures under 4% tension strain.
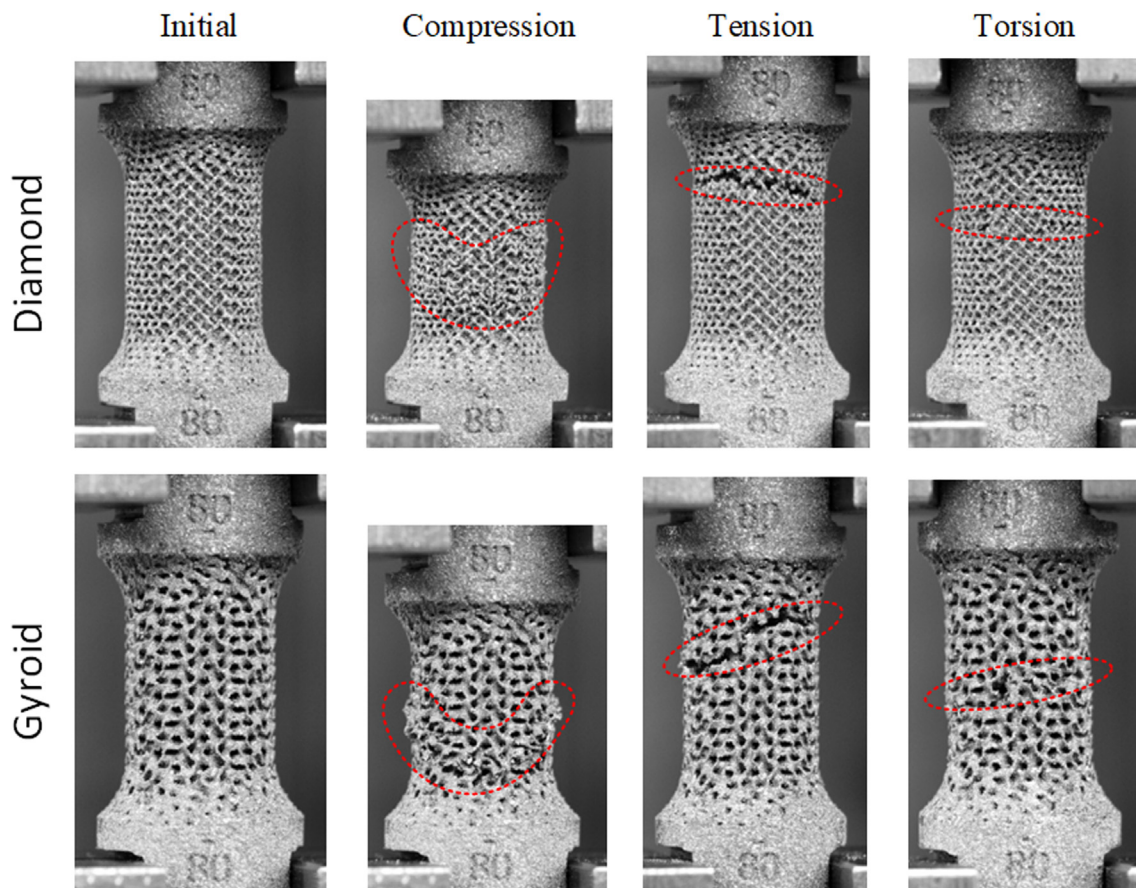

Fig. 15. Examples of specimen failure of the 80% porous diamond and gyroid structures in compression, tension and torsion. Failure regions are encircled in red. (For interpretation of the references to colour in this figure legend, the reader is referred to the web version of this article.)

yield stress relations have similar coefficient and exponent values, whereas the modulus of elasticity equations are indeed very different, with the previous study's values being much lower (coefficients of 0.09–0.20 vs 0.67–0.70, and exponents 0.9–1.7 vs 1.8–2.3). This might be explained by the fact that in this work, these values were calculated using unloading branches of the experimental stress–strain, while in the previous work, they were obtained using the loading branches, where the stiffness of the testing assembly alters the specimen apparent behavior. Another explanation is that different AM systems and testing apparatus were used, which could also have influenced the results obtained.

Finally, in the previous work, only three levels of porosity were analysed over a smaller range (59 %-76 %), thus making the fitted power laws less robust and more susceptible to changes if the properties at one of the three levels of porosity fluctuated.

Fig. 16 brings together the numerically-obtained apparent elastic moduli and yield stresses of the two studied lattice structures in compression, tension and torsion, and compares them to the range of properties of trabecular [42–46] and cortical bone [46–51]. The scarcity of studies on the mechanical properties of bones under tensile and shear loading, as well as the scatter and degree of anisotropy of the reported data makes the selection of ideal lattice
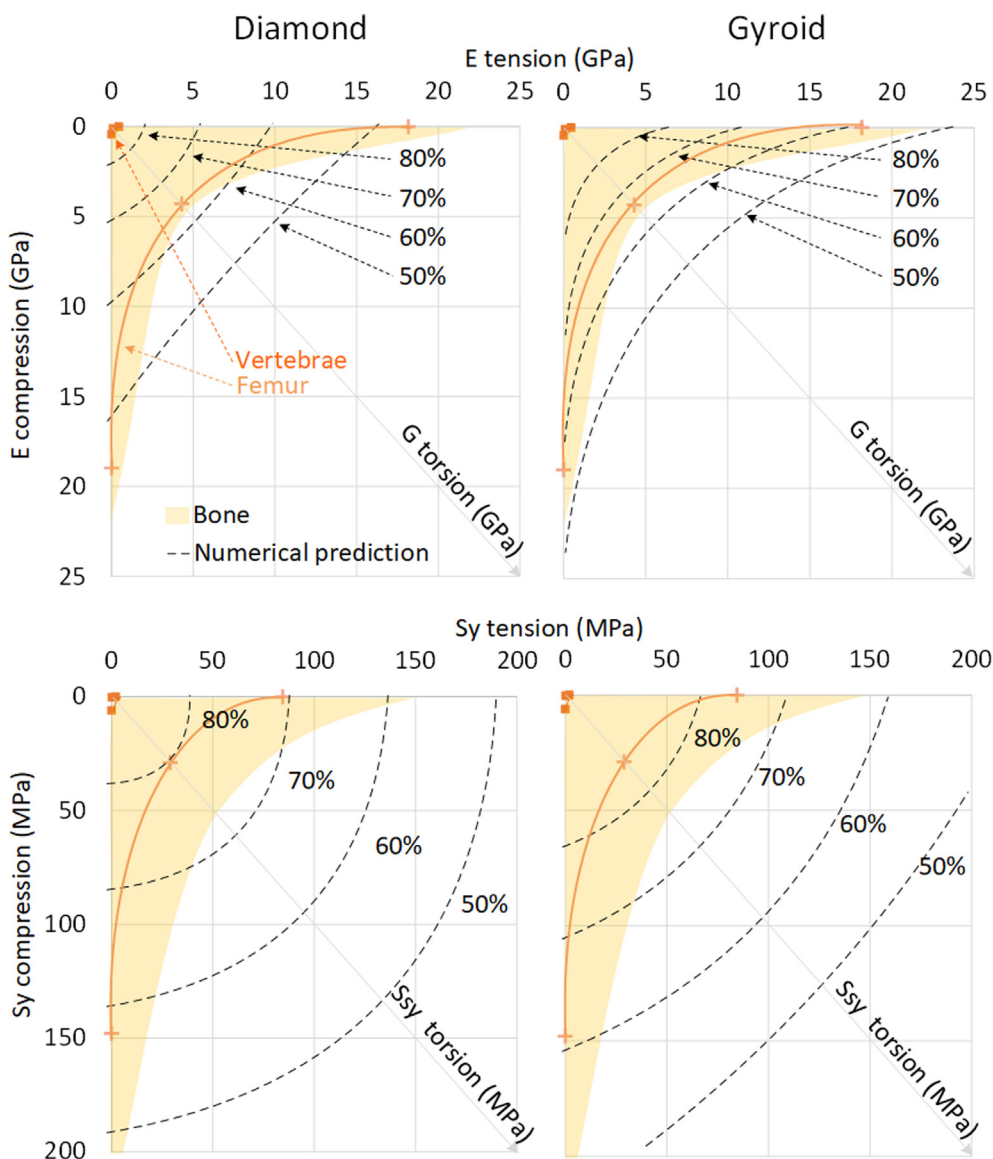
Fig. 16. Comparison of the numerically-obtained apparent elastic moduli (E and G) and yield stresses (Sy and Ssy) of the diamond and gyroid lattices for compression (vertical axis), tension (horizontal axis), and torsion (diagonal) to the range of properties of bone structures, presented as shaded zones in each diagram [42–51]. Properties of the vertebrae [52,54] and the femur [51] for the three loading modes are shown as tangible examples of the potential application requirements.

candidates challenging. For a specific application such as intervertebral cages, the lattice structures must outperform the vertebrae during flexion/extension, compression and rotation of the human spine, which have properties close to those of trabecular bone: yield stresses of 2–6 MPa and moduli of elasticity of 0.087–0.791 GPa [52–54]. It appears that all the structures studied in this work would fulfill the strength requirements for such an application, but would be too stiff to match the properties of the surrounding tissues. On the other hand, for an application where the implantation site is the femur having a yield stress ranging from 41 to 150 MPa and a modulus of elasticity ranging from 6 to 19 GPa [51], 60 % gyroid structures provide an appropriate combination of stiffness-strength characteristics.

5. Conclusions

The main goal of this work was to compare numerically and experimentally 50–80 % porosity strut-based diamond and sheet-based gyroid lattice structures for three loading modes: axial compression/tension and torsion.

- Manufactured specimens were within 0–5 % of the targeted 50–80 % porosity levels, with the highest deviations occurring at the upper bounds of porosity, where the structures approached the manufacturing limits of the AM system. Printing defects were present in the form of internal pores, geometrical discontinuities, structural distortions and surface sintered particles.
- Experimental testing showed quasi-identical behavior of the tested structures in tension and compression with elastic moduli ranging from 3 to 22 GPa and yield stresses ranging from 48 to 186 MPa. Torsional results indicate that the lattice structures do not follow the von Mises limitation theory, since the ratio between the shear and axial yield stresses is higher than the traditional 0.577 for isotropic alloys (∼0.94 for diamonds and ∼ 0.87 for gyroids).
- Numerical models of all the studied structures were developed for the three loading modes and partially validated by mechanical testing. Simulations overestimated the stiffness and yield stress of the structures by 25 % on average. These discrepancies are attributable to the uncertainty in the manufactured density, as well as to the limited representativity of the model boundary conditions.

- All studied lattice structures exhibited adequate resistance for the use in intervertebral cages. Their stiffness (3–22 GPa) was greater than those of the vertebrae (0.087–0.791 GPa), while situated in the stiffness range of cortical bone (7–22 GPa).

Data availability

The raw and processed data required to reproduce these findings cannot be shared at this time as the data also forms part of an ongoing study.

Declaration of Competing Interest

The authors declare that they have no known competing financial interests or personal relationships that could have appeared to influence the work reported in this paper.

References

[1] X.-Y. Zhang, G. Fang, J. Zhou, Additively manufactured scaffolds for bone tissue engineering and the prediction of their mechanical behavior: A review, Materials 10 (1) (2017) 50.

[2] D. Mahmoud, M. Elbestawi, Lattice structures and functionally graded materials applications in additive manufacturing of orthopedic implants: A review, Journal of Manufacturing and Materials Processing 1 (2) (2017) 13.

[3] A.A. Zadpoor, Additively manufactured porous metallic biomaterials, J. Mater. Chem. B 7 (26) (2019) 4088–4117.

[4] L.-Y. Chen, S.-X. Liang, Y. Liu, L.-C. Zhang, Additive manufacturing of metallic lattice structures: Unconstrained design, accurate fabrication, fascinated performances, and challenges, Mater. Sci. Eng. R. Rep. 146 (2021) 100648.

[5] L. Murr, Metallurgy principles applied to powder bed fusion 3D printing/additive manufacturing of personalized and optimized metal and alloy biomedical implants: an overview, J. Mater. Res. Technol. 9 (1) (2020) 1087–1103.

[6] A. Timercan, V. Sheremetyev, V. Brailovski, Mechanical properties and fluid permeability of gyroid and diamond lattice structures for intervertebral devices: functional requirements and comparative analysis, Sci. Technol. Adv. Mater. 22 (1) (2021) 285–300.

[7] Y. Tang, Y.F. Zhao, A survey of the design methods for additive manufacturing to improve functional performance, Rapid Prototyp. J. 22 (3) (2016) 569–590.

[8] L. Zhang, S. Feih, S. Daynes, S. Chang, M.Y. Wang, J. Wei, W.F. Lu, Energy absorption characteristics of metallic triply periodic minimal surface sheet structures under compressive loading, Addit. Manuf. 23 (2018) 505–515.

[9] O. Al-Ketan, R. Rowshan, R.K. Abu Al-Rub, Topology-mechanical property relationship of 3D printed strut, skeletal, and sheet based periodic metallic cellular materials, Addit. Manuf. 19 (2018) 167–183.

[10] S. Ma, Q. Tang, X. Han, Q. Feng, J. Song, R. Setchi, Y. Liu, Y. Liu, A. Goulas, D.S. Engstrøm, Manufacturability, mechanical properties, mass-transport properties and biocompatibility of TPMS scaffolds fabricated by selective laser melting, Mater. Des. 109034 (2020).

[11] A.M. Abou-Ali, O. Al-Ketan, D.-W. Lee, R. Rowshan, R.K.A. Al-Rub, Mechanical behavior of polymeric selective laser sintered ligament and sheet based lattices of triply periodic minimal surface architectures, Mater. Des. 196 (2020) 109100.

[12] O. Al-Ketan, D.-W. Lee, R. Rowshan, R.K.A. Al-Rub, Functionally graded and multi-morphology sheet TPMS lattices: Design, manufacturing, and mechanical properties, J. Mech. Behav. Biomed. Mater. 102 (2020) 103520.

[13] F. Bobbert, K. Lietaert, A.A. Eftekhari, B. Pouran, S. Ahmadi, H. Weinans, A. Zadpoor, Additively manufactured metallic porous biomaterials based on minimal surfaces: A unique combination of topological, mechanical, and mass transport properties, Acta Biomater. 53 (2017) 572–584.

[14] A. Issariyapat, S. Kariya, A. Alhazaa, J. Umeda, K. Kondoh, Additive Manufacturing and Characterization of High Strength Ti-Zr Gyroid Scaffolds Using Pre-Mixed Ti-ZrH2 Powders, JOM (2021) 1–11.

[15] C. Lu, C. Zhang, P. Wen, F. Chen, Mechanical Behavior of Al-Si10-Mg Gyroid Surface with Variable Topological Parameters Fabricated via Laser Powder Bed Fusion, J. Mater. Res. Technol. (2021).

[16] Y. Wang, X. Ren, Z. Chen, Y. Jiang, X. Cao, S. Fang, T. Zhao, Y. Li, D. Fang, Numerical and experimental studies on compressive behavior of Gyroid lattice cylindrical shells, Mater. Des. 186 (2020) 108340.

[17] S.O. Obadimu, K.I. Kourousis, Compressive Behaviour of Additively Manufactured Lattice Structures: A Review, Aerospace 8 (8) (2021) 207.

[18] G. Yu, Z. Li, S. Li, Q. Zhang, Y. Hua, H. Liu, X. Zhao, D.T. Dhaidhai, W. Li, X. Wang, The select of internal architecture for porous Ti alloy scaffold: A compromise between mechanical properties and permeability, Mater. Des. 108754 (2020).

[19] C.N. Kelly, J. Francovich, S. Julmi, D. Safranski, R.E. Guldberg, H.J. Maier, K. Gall, Fatigue Behavior of As-Built Selective Laser Melted Titanium Scaffolds with Sheet-based Gyroid Microarchitecture for Bone Tissue Engineering, Acta Biomater. (2019).

[20] A. Yánez, A. Cuadrado, O. Martel, H. Afonso, D. Monopoli, Gyroid porous titanium structures: a versatile solution to be used as scaffolds in bone defect reconstruction, Mater. Des. 140 (2018) 21–29.

[21] K. Nelson, C.N. Kelly, K. Gall, Effect of stress state on the mechanical behavior of 3D printed porous Ti6Al4V scaffolds produced by laser powder bed fusion, Mater. Sci. Eng. B 286 (2022) 116013.

[22] C. Simoneau, V. Brailovski, P. Terriault, Design, manufacture and tensile properties of stochastic porous metallic structures, Mech. Mater. 94 (2016) 26–37.

[23] G. Dong, Y. Tang, Y.F. Zhao, A survey of modeling of lattice structures fabricated by additive manufacturing, J. Mech. Des. 139 (10) (2017) 100906.

[24] N. Soro, N. Saintier, J. Merzeau, M. Veidt, M.S. Dargusch, Quasi-static and fatigue properties of graded Ti–6Al–4V lattices produced by Laser Powder Bed Fusion (LPBF), Addit. Manuf. 37 (2021) 101653.

[25] D. Ali, S. Sen, Finite element analysis of mechanical behavior, permeability and fluid induced wall shear stress of high porosity scaffolds with gyroid and lattice-based architectures, J. Mech. Behav. Biomed. Mater. 75 (2017) 262–270.

[26] H. Zhou, M. Zhao, Z. Ma, D.Z. Zhang, G. Fu, Sheet and network based functionally graded lattice structures manufactured by selective laser melting: Design, mechanical properties, and simulation, Int. J. Mech. Sci. 105480 (2020).

[27] L.J. Gibson, Biomechanics of cellular solids, J. Biomech. 38 (3) (2005) 377–399.

[28] Food and Drug Administration, Class II Special Controls Guidance Document, 2007.

[29] H. Kienapfel, C. Sprey, A. Wilke, P. Griss, Implant fixation by bone ingrowth, J. Arthroplasty 14 (3) (1999) 355–368.

[30] N. Taniguchi, S. Fujibayashi, M. Takemoto, K. Sasaki, B. Otsuki, T. Nakamura, T. Matsushita, T. Kokubo, S. Matsuda, Effect of pore size on bone ingrowth into porous titanium implants fabricated by additive manufacturing: an in vivo experiment, Mater. Sci. Eng. C 59 (2016) 690–701.

[31] D. Hara, Y. Nakashima, T. Sato, M. Hirata, M. Kanazawa, Y. Kohno, K. Yoshimoto, Y. Yoshihara, A. Nakamura, Y. Nakao, Bone bonding strength of diamond-structured porous titanium-alloy implants manufactured using the electron beam-melting technique, Mater. Sci. Eng. C 59 (2016) 1047–1052.

[32] M. Dumas, P. Terriault, V. Brailovski, Modelling and characterization of a porosity graded lattice structure for additively manufactured biomaterials, Mater. Des. 121 (2017) 383–392.

[33] ISO13314, Mechanical testing of metals — Ductility testing — Compression test for porous and cellular metals, 2011.

[34] ASTM, E143-20 Standard Test Method for Shear Modulus at Room Temperature, (2021).

[35] ASTM, F2450-18 Standard Guide for Assessing Microstructure of Polymeric Scaffolds for Use in Tissue-Engineered Medical Products, 2018.

[36] S.E. Brika, M. Letenneur, C.A. Dion, V. Brailovski, Influence of particle morphology and size distribution on the powder flowability and laser powder bed fusion manufacturability of Ti-6Al-4V alloy, Addit. Manuf. 31 (2020) 100929.

[37] D. Downing, A. Jones, M. Brandt, M. Leary, Increased efficiency gyroid structures by tailored material distribution, Mater. Des. 197 (2021) 109096.

[38] L.J. Gibson, M.F. Ashby, B.A. Harley, Cellular Materials in Nature and Medicine, Cambridge University Press, 2010.

[39] H. Salem, L. Carter, M. Attallah, H. Salem, Influence of processing parameters on internal porosity and types of defects formed in Ti6Al4V lattice structure fabricated by selective laser melting, Mater. Sci. Eng. A 767 (2019) 138387.

[40] S.L. Sing, F.E. Wiria, W.Y. Yeong, Selective laser melting of lattice structures: A statistical approach to manufacturability and mechanical behavior, Rob. Comput. Integr. Manuf. 49 (2018) 170–180.

[41] J. Suryawanshi, G. Singh, S. Msolli, M.H. Jhon, U. Ramamurty, Tension-compression asymmetry and shear strength of titanium alloys, Acta Mater. 221 (2021) 117392.

[42] J. Galante, W. Rostoker, R. Ray, Physical properties of trabecular bone, Calcif. Tissue Res. 5 (1) (1970) 236–246.

[43] N.S. Hakim, A.I. King, A three dimensional finite element dynamic response analysis of a vertebra with experimental verification, J. Biomech. 12 (4) (1979) 277–292.

[44] C.M. Ford, T.M. Keaveny, The dependence of shear failure properties of trabecular bone on apparent density and trabecular orientation, J. Biomech. 29 (10) (1996) 1309–1317.

[45] M. Kasra, M.D. Grynpas, On shear properties of trabecular bone under torsional loading: effects of bone marrow and strain rate, J. Biomech. 40 (13) (2007) 2898–2903.

[46] X. Wang, S. Xu, S. Zhou, W. Xu, M. Leary, P. Choong, M. Qian, M. Brandt, Y.M. Xie, Topological design and additive manufacturing of porous metals for bone scaffolds and orthopaedic implants: A review, Biomaterials 83 (2016) 127–141.

[47] U. Wolfram, J. Schwiedrzik, Post-yield and failure properties of cortical bone, BoneKEy reports 5 (2016).

[48] N.H. Hart, S. Nimphius, T. Rantalainen, A. Ireland, A. Siafarikas, R. Newton, Mechanical basis of bone strength: influence of bone material, bone structure and muscle action, J. Musculoskelet. Neuronal Interact. 17 (3) (2017) 114.

[49] C. Turner, T. Wang, D. Burr, Shear strength and fatigue properties of human cortical bone determined from pure shear tests, Calcif. Tissue Int. 69 (6) (2001).

[50] T. Tang, V. Ebacher, P. Cripton, P. Guy, H. McKay, R. Wang, Shear deformation and fracture of human cortical bone, Bone 71 (2015) 25–35.

[51] M.J. Mirzaali, J.J. Schwiedrzik, S. Thaiwichai, J.P. Best, J. Michler, P.K. Zysset, U. Wolfram, Mechanical properties of cortical bone and their relationships with age, gender, composition and microindentation properties in the elderly, Bone 93 (2016) 196–211.

[52] K. Singer, S. Edmondston, R. Day, P. Breidahl, R. Price, Prediction of thoracic and lumbar vertebral body compressive strength: correlations with bone mineral density and vertebral region, Bone 17 (2) (1995) 167–174.

[53] F. El Masri, E. Sapin de Brosses, K. Rhissassi, W. Skalli, D. Mitton, Apparent Young's modulus of vertebral cortico-cancellous bone specimens, Comput. Methods Biomech. Biomed. Eng. 15 (1) (2012) 23–28.

[54] U. Wolfram, H.-J. Wilke, P.K. Zysset, Valid μ finite element models of vertebral trabecular bone can be obtained using tissue properties measured with nanoindentation under wet conditions, J. Biomech. 43 (9) (2010) 1731–1737.